Monthly Notices
of the
ROYAL ASTRONOMICAL SOCIETY

Mon. Not. R. Astron. Soc. **402,** 1099–1110 (2010) doi:10.1111/j.1365-2966.2009.15937.x

Sinking of a magnetically confined mountain on an accreting neutron star

K. Wette,[1⋆] M. Vigelius[2] and A. Melatos[2]

[1] *Centre for Gravitational Physics, Australian National University, Canberra, ACT 0200, Australia*
[2] *School of Physics, University of Melbourne, Parkville, VIC 3010, Australia*

Accepted 2009 October 26. Received 2009 October 11; in original form 2009 June 13

ABSTRACT

We perform ideal-magnetohydrodynamic axisymmetric simulations of magnetically confined mountains on an accreting neutron star, with masses $\lesssim 0.12\,\mathrm{M}_\odot$. We consider two scenarios, in which the mountain sits atop a hard surface or sinks into a soft, fluid base. We find that the ellipticity of the star, due to a mountain grown on a hard surface, approaches $\sim 2 \times 10^{-4}$ for accreted masses $\gtrsim 1.2 \times 10^{-3}\,\mathrm{M}_\odot$, and that sinking reduces the ellipticity by between 25 and 60 per cent. The consequences for gravitational radiation from low-mass X-ray binaries are discussed.

Key words: accretion, accretion discs – stars: magnetic fields – stars: neutron – pulsars: general.

1 INTRODUCTION

The magnetic dipole moment μ of a neutron star is observed to diminish in the long term as the star accretes (Taam & van den Heuvel 1986; van den Heuvel & Bitzaraki 1995), although Wijers (1997) argued that μ may also be a function of parameters other than the accreted mass M_a. The μ–M_a correlation has been ascribed to a number of physical mechanisms (Melatos & Phinney 2001; Cumming 2005). First, the magnetic field may be dissipated in the stellar crust by Ohmic decay, accelerated by heating as the accreted plasma impacts upon the star (Konar & Bhattacharya 1997; Brown & Bildsten 1998; Urpin, Geppert & Konenkov 1998; Cumming, Arras & Zweibel 2004). Secondly, magnetic flux tubes may be dragged from the superconducting core by the outward motion of superfluid vortices, as the star spins down (Srinivasan et al. 1990; Ruderman, Zhu & Chen 1998; Konar & Bhattacharya 1999; Konenkov & Geppert 2001). Thirdly, the magnetic field may be screened by accretion-induced currents within the crust (Bisnovatyi-Kogan & Komberg 1974; Blondin & Freese 1986; Lovelace, Romanova & Bisnovatyi-Kogan 2005). In particular, the field may be *buried* under a mountain of accreted plasma channelled on to the magnetic poles. When M_a is large enough, the mountain spreads laterally, transporting the polar magnetic flux towards the equator (Hameury et al. 1983; Romani 1990; Brown & Bildsten 1998; Cumming, Zweibel & Bildsten 2001; Melatos & Phinney 2001; Choudhuri & Konar 2002; Payne & Melatos 2004; Zhang & Kojima 2006; Payne & Melatos 2007; Vigelius & Melatos 2008, 2009b).

Payne & Melatos (2004) computed the unique sequence of self-consistent, ideal-magnetohydrodynamic (ideal-MHD) equilibria that describes the formation of a polar mountain by magnetic burial as a function of M_a. They found that the accreted mountain is confined by the equatorially compressed magnetic field, which was unaccounted for in previous calculations, and that $10^{-5}\,\mathrm{M}_\odot$ must be accreted to lower μ by 10 per cent. Surprisingly, mountains are stable with respect to axisymmetric ideal-MHD perturbations; they oscillate globally in a superposition of acoustic and Alfvén modes but remain intact due to magnetic line-tying at the stellar surface (Payne & Melatos 2007). The same equilibria are susceptible to non-axisymmetric, Parker-like instabilities (specifically the gravitationally driven, undular submode), but the instability preserves a polar mountain when it saturates, despite reducing the mass ellipticity by ∼30 per cent (Vigelius & Melatos 2008). Recently, Vigelius & Melatos (2009b) considered resistive effects. They found that the mountain does not relax appreciably for realistic resistivities over the lifetime of a low- or high-mass X-ray binary either by global diffusion, resistive g-mode instabilities, or reconnection in the equatorial magnetic belt. The Hall drift, which exerts a destabilizing influence in isolated neutron stars (see, e.g. Rheinhardt & Geppert 2002), is unlikely to be important in accreting neutron stars due to crustal impurities (Cumming et al. 2004; Cumming 2005).

The investigations outlined in the previous paragraph suffer from two limitations. First, the mountain is assumed to rest upon a rigid surface. Under this assumption, the accreting plasma cannot sink into the stellar crust. This is unrealistic. During magnetic burial, frozen-in magnetic flux is redistributed slowly within the neutron star by the accreted plasma, as it sinks beneath the surface and spreads laterally. Choudhuri & Konar (2002) showed that the time-scale and end state of burial are tied to these slow interior motions. Secondly, the accreted plasma is assumed to satisfy an isothermal equation of state. This is an accurate model only for neutron stars with low-accretion rates $\dot{M}_\mathrm{a} \lesssim 10^{-10}\,\mathrm{M}_\odot\mathrm{yr}^{-1}$; the thermodynamics of neutron stars accreting near the Eddington limit

⋆E-mail: karl.wette@anu.edu.au

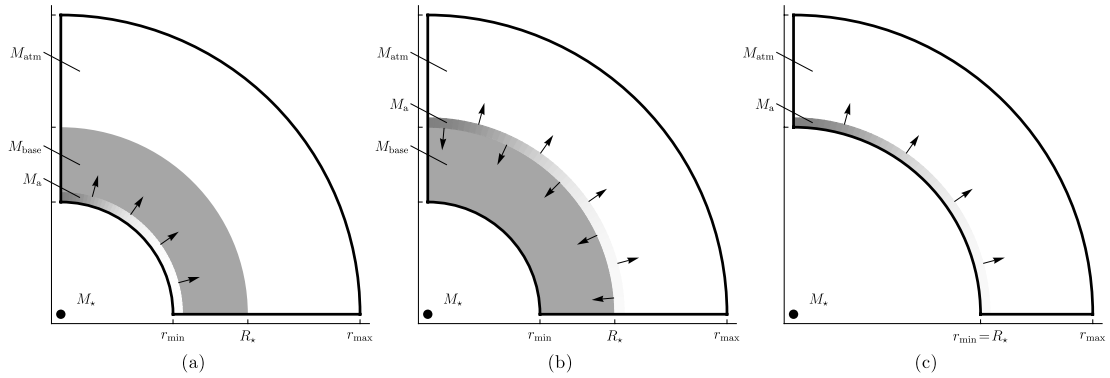

Figure 1. Diagrams illustrating schematically three mountain growth scenarios. The simulation region is bounded by $r_{\rm min} \le r \le r_{\rm max}, 0 \le \theta \le \pi/2$ (thick lines), and represents a quadrant of the star. Boundary conditions assume symmetry about $\theta = 0$ and reflection at $\theta = \pi/2$. The surface of the star is located at $r = R_\star$. Three subregions are identified. The fluid interior beneath the surface, containing mass $M_{\rm base}$, is shaded grey. The region where the mountain mass $M_{\rm a}$ is injected into the simulation is shaded in a grey to white gradient; the grey is proportional to the injected flux (see equation 4) as a function of θ. The outer atmosphere of the star, containing mass $M_{\rm atm}$, is unshaded. A central gravitational point source is labelled with its mass $M_\star$. For mountains grown on a fluid base, $M_{\rm a}$ can be injected (a) at the inner boundary $r = r_{\rm min}$ or (b) at the stellar surface $r = R_\star$. For mountains grown on a hard surface, (c) there is no fluid interior; the inner boundary is identical to the stellar surface $r = r_{\rm min} = R_\star (M_{\rm base} = 0)$. See the text in Section 2.3.

($\sim 10^{-8}\,{\rm M}_\odot\,{\rm yr}^{-1}$) is more complicated, with a depth-dependent adiabatic index (Brown & Bildsten 1998; Brown 2000). The equation of state affects the growth rate of Parker-like instabilities (Kosiński & Hanasz 2006).

In this paper, we seek to overcome the first limitation. In Section 2, we present a new method of computationally simulating the growth of a magnetic mountain with $M_{\rm a} \lesssim 0.1\,{\rm M}_\odot$. In Section 3, we compare the structure of mountains grown on hard and soft surfaces to evaluate the role of sinking. In Section 4, the resulting mass quadrupole moment is evaluated as a function of $M_{\rm a}$ for hard and soft surfaces. A comparison with the results of Choudhuri & Konar (2002) and the implications for gravitational wave emission from rapidly rotating accretors (e.g. low-mass X-ray binaries) are discussed in Section 5.

2 GROWING A REALISTICALLY SIZED MOUNTAIN BY INJECTION

In order to investigate how a magnetically confined mountain sinks into the stellar crust, we need a numerical method capable of building a stable mountain, with a realistic $M_{\rm a}$, on top of a fluid base. The approach we take builds upon previous work by Payne & Melatos (2004, 2007) and Vigelius & Melatos (2008, 2009a). Here, as a service to the reader, we briefly recapitulate the physical arguments and key results from these previous papers, with references to the relevant sections and equations.

In Payne & Melatos (2004), axisymmetric magnetic mountain equilibria are computed by solving an elliptic partial differential equation: the Grad–Shadranov equation describing hydromagnetic force balance in axisymmetric geometry (Payne & Melatos 2004, section 2.1 and equation 12). The calculation ensures that the mass-magnetic flux distribution $\partial M/\partial\psi$ is treated self-consistently: the final $\partial M/\partial\psi$ is equal to the initial $\partial M/\partial\psi$ together with the mass-flux distribution of the accreted matter, $\partial M_{\rm a}/\partial\psi$, which is characterized by the parameter $\psi_{\rm a}$ (Payne & Melatos 2004, section 2.2 and equation 13). In the limit of small $M_{\rm a}$, the final equilibrium flux solution is characterized by the ratio $M_{\rm a}/M_{\rm c}$, where the characteristic mass $M_{\rm c} \propto M_\star R_\star^2 B_\star^2$ is the accreted mass required to halve μ (Payne & Melatos 2004, section 3.2 and equation 30; Payne & Melatos 2007, section 2.2 and equation 3). The characteristic mass contains the dependence of the equilibrium solution on the parameters of the neutron star, in particular the magnetic field strength $B_\star$. The Grad–Shafranov equilibria are computed using an iterative numerical solver (Payne & Melatos 2004, section 3.3); this approach only converges numerically for low accreted masses $M_{\rm a} \le M_{\rm c} \approx 10^{-4}\,{\rm M}_\odot$ (Payne & Melatos 2004, section 3.4), and it fails to accommodate a fluid interior within its fixed-boundary framework.[1]

In Payne & Melatos (2007) and Vigelius & Melatos (2008), Grad–Shafranov equilibria are loaded into ZEUS, a multipurpose, time-dependent, ideal-MHD solver (Stone & Norman 1992a,b; Hayes et al. 2006), and further evolved in axisymmetric (Payne & Melatos 2007) and three-dimensional geometries (Vigelius & Melatos 2008). The characteristic mass $M_{\rm c}$ is used to reduce the length-scales of the simulated neutron star to circumvent numerical difficulties and render the simulations computationally tractable (Payne & Melatos 2007, section 3.3; Vigelius & Melatos 2008, section 2.3 and equation 6, and section 4.6). Two approaches are explored to augmenting the mass of a Grad–Shafranov mountain, up to $M_{\rm a} \lesssim 5.6 M_{\rm c}$: in the first approach, additional matter is injected through the outer boundary along the polar flux tube $0 \le \psi \le \psi_{\rm a}$ (Payne & Melatos 2007, section 4.2); in the second approach, the density of the mountain is uniformly increased at every point, while the magnetic field is preserved (Payne & Melatos 2007, section 4.4). A plausible attempt to extend this latter approach to include sinking is outlined in Appendix A; ultimately, this attempt proved unsuccessful, and was abandoned. Instead, the method presented in this section uses ZEUS-MP (Hayes et al. 2006) to build magnetic mountain equilibria from scratch; this approach was first proposed in Vigelius & Melatos (2009a).

2.1 Outline of the method

The setup of the simulations presented in this paper is described schematically in Fig. 1. Three numerical experiments are

[1] In Payne & Melatos (2004), the Grad–Shafranov equation is solved subject to Dirichlet and Neumann conditions at *fixed* boundaries. Mathematically, one can formulate a well-posed boundary-value problem for the Grad–Shafranov equation in the presence of a *free* boundary, e.g. the sinking base of a mountain; in practice, however, this is an extremely difficult problem to solve.

performed: growing on to a hard surface, growing on to a soft surface by injecting matter from below, and repeating the latter experiment by injecting matter at some altitude.

To simulate accretion, we inject matter from below, through the inner boundary of the simulation at $r = r_{\rm min}$. One might expect a realistic simulation of accretion to add matter from above, through the outer boundary $r = r_{\rm max}$. The two scenarios are, however, equivalent in ideal MHD; the magnetic field is frozen into the fluid, which is thus constrained to move along lines of magnetic flux. Provided that the simulation reaches equilibrium, it becomes inconsequential, with respect to ideal MHD, through which end of a flux tube matter is added. This is because matter cannot cross flux surfaces in ideal MHD, so the mass column $\mathrm{d}M(\psi)$ between ψ and $\psi + \delta\psi$ adjusts to reach the same hydrostatic radial profile *in equilibrium*, whether it enters slowly from below or falls slowly from above. In the presence of gravity, which (in the case of a sinking mountain) induces steep density gradients in the fluid base, the results to be presented in Section 3.3 confirm that this situation remains true; two different injection scenarios (described below) give ellipticities consistent to within 10 per cent. There remains, however, the subtle and difficult question of irreversible magnetic reconnection at the grid corners, which remains unresolved (see the discussion in Section 3.4).

In practice, it is advantageous to add matter through the inner boundary, because we wish to inject along particular flux tubes, and this is easiest to do at $r = r_{\rm min}$, where the magnetic footprints are fixed in place (unlike at $r = r_{\rm max}$). This constraint, known as magnetic line tying, contributes to the stability of the mountain (Goedbloed & Poedts 2004; Vigelius & Melatos 2008). It is well justified physically, provided that $r_{\rm min}$ lies deep enough within the star, so that the fluid base (and frozen-in magnetic flux) remains relatively stationary, and is not significantly perturbed by the spreading and sinking of the mountain. This is the case if the mass $M_{\rm base}$ of the fluid base, initially in the region $r_{\rm min} < r < R_\star$, is much greater than $M_{\rm a}$. To confirm that the mountain does not greatly push the crustal material, we first calculate the fraction of $M_{\rm base}$ contained in each grid cell, and then determine the change in this quantity between the initial and final times of the simulation; this gives the change in the spatial distribution of $M_{\rm base}$ over the simulation, as a function of the grid cell. For all simulations with sinking, the median change in $M_{\rm base}$, over all grid cells, is on average $\sim$10 per cent. Thus, the distribution of the fluid base does not change much during accretion. Recent molecular dynamics simulations of crystalline neutron matter, which predict a high breaking strain $\sim$0.1 (Horowitz & Kadau 2009), also support the line-tying hypothesis.

When a mountain is grown on to a fluid base $M_{\rm base}$, a difficulty arises. ZEUS-MP models a single fluid, with a unique velocity field (Hayes et al. 2006); there is no facility for simulating the movement of one fluid, the injected mountain, with respect to another fluid, the stationary crust.[2] We are left with two alternatives: to assign the same velocity to the injected mountain and the crust (the behaviour of ZEUS-MP's 'inflow' boundary condition) or to assign a negligible or zero velocity to the injected mountain, in order to keep the base stationary. In the first case, ZEUS-MP fails catastrophically for desirable values of the injection velocity ($\gtrsim$5 per cent of the escape velocity). In the second case, which we study in Section 3, mountains remain subterranean and never rise to the stellar surface $r = R_\star$. As a check, therefore, we examine two scenarios: injection at $r = r_{\rm min}$ and $r = R_\star$. We show in Section 3.3 that the results in both scenarios are quantitatively alike, confirming their robustness.

Throughout this paper, we adopt the viewpoint that the accreted matter and the mountain are one and the same; the accreted mass and the mass of the mountain are identical and are both denoted by $M_{\rm a}$. This is a matter of terminology, not physics. There is no 'hard edge' to the mountain; matter is accreted on all flux surfaces $0 \leq \psi \leq \psi_\star$ (see equation 4 in Section 2.3), not just on the polar cap $0 \leq \psi \leq \psi_{\rm a}$, which contains $\sim$63 per cent of $M_{\rm a}$. Under the assumption of ideal MHD, matter cannot spread across flux surfaces, i.e. there is no Ohmic diffusion. We also do not model the accreted matter once it has sunk beyond the crust, as do e.g. Choudhuri & Konar (2002); see the discussion in Section 5.

2.2 Initial setup

The initial setup of our simulations closely follows Payne & Melatos (2007) and Vigelius & Melatos (2008). The setup of ZEUS-MP[3] is through a set of parameters which control: the geometry of the problem, the physical phenomena to be modelled (e.g. MHD, gravity), the simulation grid and its boundary conditions, the equation of state, and the choice of time-step. Appropriate values for these parameters are given in Payne & Melatos (2007), section 3 and appendix A1, and in Vigelius & Melatos (2008), sections 2.2–2.3 and appendix A.

To avoid numerical difficulties with steep magnetic field gradients, we simulate a scaled-down neutron star, where the mass $M_\star$ and radius $R_\star$ are artificially reduced, while the hydrostatic scale-height $h_0 = c_{\rm s}^2 R_\star^2 / G M_\star$ is kept constant (Payne & Melatos 2007). The down-scaling transformation preserves the equilibrium shape of the mountain exactly in the small-$M_{\rm a}$ limit (Payne & Melatos 2004, 2007) and has been validated approximately for $M_{\rm a} \lesssim 20 M_{\rm c}$ (Vigelius & Melatos 2008). We use dimensionless units within ZEUS-MP, setting the isothermal sound $c_{\rm s}$ and gravitational constant G to unity, and adopting h_0 as the unit of length. Table 1 explains how to convert between an astrophysical neutron star, the scaled-down model, and dimensionless ZEUS-MP units.

The simulations are performed on an axisymmetric rectangular grid with N_r cells spaced logarithmically in r, and $N_\theta = 64$ cells spaced linearly in θ. The logarithmic spacing in r is determined by the ratio $\Delta r_{N_r-1}/\Delta r_0$ of the maximum to minimum radial grid spacing (see Appendix B). This ratio is chosen large enough to concentrate on grid resolution near the inner boundary, but small enough to ensure reasonable run times. We set $r_{\rm max} = 1.2 R_\star = 60\, h_0$ to give the mountain ample room to expand without meeting the outer boundary, and stipulate reflecting boundary conditions at $\theta = 0$ and $\theta = \pi/2$, 'inflow' boundary conditions at $r = r_{\rm min}$, and 'outflow' boundary conditions at $r = r_{\rm max}$; more details can be found in Payne & Melatos (2007). The magnetic field is initially that of a dipole, and $B_\star$ is its magnitude at the polar surface.

A gravitational point source $M_\star$ is placed at $r = 0$, and self-gravity is ignored. The density field is initialized to be the static atmosphere of an isothermal fluid with no self-gravity,

$$\rho(t = 0, r) = \rho_{R_\star} \exp\left[\frac{G M_\star}{c_{\rm s}^2}\left(\frac{1}{r} - \frac{1}{R_\star}\right)\right]. \quad (1)$$

Ideally, the region $r > R_\star$ should start evacuated, but ZEUS-MP requires the density to be non-zero everywhere, so we set $M_{\rm atm} = 5 \times 10^{-6}\,{\rm M}_\odot$ (approximately 4 per cent of the mass of the smallest

[2] ZEUS-MP can track the concentrations of comoving components within the same fluid; we exploit this in Section 2.3.

[3] Version 2.1.2, available from http://lca.ucsd.edu/portal/codes/zeusmp2.

Table 1. Conversion of physical quantities into dimensionless variables in the simulations. Physical quantities are first converted to their values in the scaled-down model by multiplying by $[a(\text{Simulation})/a(\text{Astrophysical neutron star})]^n$, where $a = R_\star/h_0$ parametrizes the curvature down-scaling, and n is listed in Column 4. Scaled-down physical quantities are then re-expressed in the dimensionless units of ZEUS-MP according to Column 6. The table is divided into three horizontal parts containing: stellar parameters (Payne & Melatos 2004), simulation control parameters (see Fig. 1) and simulation outputs.

Quantity	Symbol	Astrophysical neutron star	Down-scaling index n	Simulation	ZEUS-MP dimensionless unit
Scaling ratio	a	1.9×10^4	None	50	None
Stellar mass	$M_\star$	$1.4\,\mathrm{M}_\odot$	2	$10^{-5}\,\mathrm{M}_\odot$	$M_0 = c_\mathrm{s}^2 h_0/G = 8.1 \times 10^{24}\,\mathrm{g}$
Stellar radius	$R_\star$	$10^6\,\mathrm{cm}$	1	$2.7 \times 10^3\,\mathrm{cm}$	$h_0 = c_\mathrm{s}^2 R_\star^2/GM_\star = 54\,\mathrm{cm}$
Stellar magnetic field	$B_\star$	$10^{12}\,\mathrm{G}$	None		$B_0 = c_\mathrm{s}^2/G^{1/2}h_0 = 7.2 \times 10^{17}\,\mathrm{G}$
Isothermal sound speed	c_s	$10^8\,\mathrm{cm\,s^{-1}}$	None		c_s
Critical mass	M_c	$1.2 \times 10^{-4}\,\mathrm{M}_\odot$	4	$6.1 \times 10^{-15}\,\mathrm{M}_\odot$	M_0
Inner boundary	r_min		1	see Table 2	h_0
Outer boundary	r_max		1	$1.2R_\star$	h_0
Accreted mass	M_a		4	see Table 2	M_0
Mass of outer atmosphere	M_atm		4	$5 \times 10^{-6}\,\mathrm{M}_\odot$	M_0
Mass of fluid base	M_base		4	$10M_\mathrm{a}$	M_0
Mountain density	$\rho \mathrm{X}_\mathrm{a}$		1		$\rho_0 = M_0/h_0^3 = 5.2 \times 10^{19}\,\mathrm{g\,cm^{-3}}$
Magnetic field	$\boldsymbol{B}$		None		B_0
Ellipticity	ϵ		2		None
Time	t		None		$t_0 = h_0/c_\mathrm{s} = 5.4 \times 10^{-7}\,\mathrm{s}$

Table 2. Simulations of magnetic mountains presented in this paper. The accompanying parameters are: the target accreted mass M_a, in units of M_c and $\mathrm{M}_\odot$; the number of grid cells in the r direction N_r; the radius of the inner radial boundary r_min; the ratio of the maximum to minimum radial grid spacing $\Delta r_{N_r-1}/\Delta r_0$; the injection radius r_inj; the injection velocity v_inj; the injection time T_a and the total (successfully completed) simulation time t_max.

Simulation	$\frac{M_\mathrm{a}}{M_\mathrm{c}}$	$\frac{M_\mathrm{a}}{\mathrm{M}_\odot}$	N_r	$\frac{r_\mathrm{min}}{h_0}$	$\frac{\Delta r_{N_r-1}}{\Delta r_0}$	r_inj	$\frac{v_\mathrm{inj}}{c_\mathrm{s}}$	$\frac{T_\mathrm{a}}{t_0}$	$\frac{t_\mathrm{max}}{T_\mathrm{a}}$
$\mathcal{H}(1)$	1	1.2×10^{-4}	64	50.0	200	$r_\mathrm{min} = R_\star$	10^{-4}	5×10^3	1.5
$\mathcal{H}(10)$	10	1.2×10^{-3}	64	50.0	200	$r_\mathrm{min} = R_\star$	10^{-4}	5×10^3	1.5
$\mathcal{H}(10^2)$	100	1.2×10^{-2}	64	50.0	200	$r_\mathrm{min} = R_\star$	10^{-4}	5×10^3	1.5
$\mathcal{H}(10^3)$	1000	1.2×10^{-1}	64	50.0	200	$r_\mathrm{min} = R_\star$	10^{-4}	5×10^3	1.5
$\mathcal{S}(r_\mathrm{min}, 1)$	1	1.2×10^{-4}	96	44.7	306	r_min	0	5×10^3	1.5
$\mathcal{S}(r_\mathrm{min}, 10)$	10	1.2×10^{-3}	112	42.8	344	r_min	0	5×10^3	1.5
$\mathcal{S}(r_\mathrm{min}, 10^2)$	100	1.2×10^{-2}	120	41.1	378	r_min	0	5×10^3	1.5
$\mathcal{S}(r_\mathrm{min}, 10^3)$	1000	1.2×10^{-1}	128	39.5	410	r_min	0	5×10^3	1.5
$\mathcal{S}(R_\star, 1)$	1	1.2×10^{-4}	96	44.7	306	$R_\star$	0	5×10^3	1.5
$\mathcal{S}(R_\star, 10)$	10	1.2×10^{-3}	112	42.8	344	$R_\star$	0	1×10^4	1.5
$\mathcal{S}(R_\star, 10^2)$	100	1.2×10^{-2}	120	41.1	378	$R_\star$	0	2×10^4	1.5
$\mathcal{S}(R_\star, 10^3)$	1000	1.2×10^{-1}	128	39.5	410	$R_\star$	0	8×10^4	0.35

mountain; see Table 2). Integrating equation (1) over the region $r > R_\star$ (see Fig. 1) fixes the density at the stellar surface $\rho_{R_\star}$ in terms of M_atm. In contrast, we require the mass of the fluid base M_base (when a soft surface is being modelled) to be much larger than the mass of the mountain, as discussed in Section 2.1. In all runs, we choose $M_\mathrm{base}/M_\mathrm{a} \approx 10$. Integrating equation (1) over the region containing M_base then fixes r_min.

2.3 Injection procedure

ZEUS-MP's 'inflow' boundary condition permits injection at the edge of the simulation volume. To enable injection at $r = R_\star$, as in Fig. 1(b), we implement a more flexible custom procedure, and use the built-in 'inflow' condition only to tie the magnetic flux at $r = r_\mathrm{min}$. We describe the procedure briefly below; further details are in Appendix C.

We inject mass M_a into an injection region $r_\mathrm{inj} < r < r_\mathrm{inj} + \delta r_\mathrm{inj}$, $0 < \theta < \pi/2$, over a time interval $0 < t < T_\mathrm{a}$. (We set $\delta r_\mathrm{inj} = 0.1\ h_0$ throughout.) The flux of accreted matter at time t entering a point (r, θ) in the injection region is given by

$$\frac{\partial^3 M_\mathrm{a}}{\partial t \partial r \partial \theta}(t, r, \theta) \propto \dot{M}_\mathrm{a}(t) \frac{\partial M_\mathrm{a}}{\partial \psi}(r, \theta), \tag{2}$$

where we choose

$$\dot{M}_\mathrm{a}(t) \propto t^2 (T_\mathrm{a} - t)^2\,, \tag{3}$$

and

$$\frac{\partial M_\mathrm{a}}{\partial \psi}(r, \theta) \propto \exp(-bR_\star r^{-1} \sin^2\theta)\,. \tag{4}$$

The normalization of equation (2) is chosen so that, for each simulation, the mass of the mountain is equal to M_a at time $t = T_\mathrm{a}$, i.e. $M_\mathrm{a}(t = T_\mathrm{a}) \equiv M_\mathrm{a}$. After time $t = T_\mathrm{a}$, no further mass is added, but

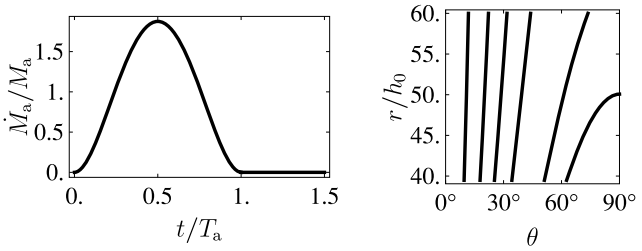

Figure 2. Left-hand panel: the accretion rate $\dot{M}_a(t)$, given by equation (3). Right-hand panel: the initial mass-flux distribution $\partial M/\partial\psi$, given by equation (4). Contours are at (right- to left-hand panels) 0.05, 0.1, 0.3, 0.5, 0.7 and 0.9 of the maximum.

we evolve the system up to $t = t_{\max} = 1.5T_a$ to test the stability of the mountain obtained.

Equation (3) determines the rate of accretion; it is plotted in Fig. 2 (left-hand panel). The functional form was chosen to ensure numerical stability in ZEUS-MP, and has no particular astrophysical justification, except to ensure that a mountain builds up to its target mass smoothly over the time-scale T_a. For this reason, it is a smooth bell-shaped function, designed to avoid any discontinuity in the accretion rate, which might excite undesired oscillations in the fluid or provoke numerical instabilities.

Equation (4) gives a mass-flux distribution consistent with that of Payne & Melatos (2004); it is plotted in Fig. 2 (right-hand panel). It does not attempt to model the interaction of the accreted matter with the magnetosphere, from which the mass-flux distribution would originate; instead, it is chosen such that the majority (∼63 per cent) of the accreted matter falls on the polar cap $0 \le \psi \le \psi_a$. The parameter $b = \psi_\star/\psi_a = 3$ determines the polar cap radius $R_\star \sin^{-1}(b^{-1/2})$. It is determined astrophysically by disc-magnetosphere force balance, and is related to the stellar magnetic field via $b \propto \psi_\star \propto B_\star$ (Payne & Melatos 2004). In this theoretical paper, however, we treat b (and therefore $B_\star$) as a free parameter, and do not attempt a self-consistent solution of the disc-magnetosphere system (see, e.g. Romanova, Kulkarni & Lovelace 2008). With this freedom, b is chosen unrealistically large to preserve numerical stability (Payne & Melatos 2004).

We use ZEUS-MP's multispecies tracking facility (Hayes et al. 2006) to record, throughout the simulation, the fraction of the density, $0 \le X_a(t, r, \theta) \le 1$, that originates from accretion (i.e. added at $t > 0$ via the injection procedure), as opposed to from the initial configuration at $t = 0$. This allows us to track the spread of the mountain independently of the motion of the remaining (displaced) stellar matter.

We require that the mountain grows quasi-statically, in the sense that the accretion time-scale T_a is always much greater than $t_{\text{Alfvén}}$, the characteristic pole-equator crossing time of an Alfvén wave. Following Vigelius & Melatos (2008), we compute the crossing time at $t = 0, r = R_\star$: from the Alfvén speed $v_{\text{Alfvén}} = B_\star/(4\pi\rho_{R_\star})^{1/2} \approx 0.2c_s$ (see Table 1), we obtain $t_{\text{Alfvén}} = \pi R_\star/(2v_{\text{Alfvén}}) \approx 400t_0$. The condition $t_{\text{Alfvén}} \ll T_a$ is verified by comparison with the values for T_a listed in Table 2. The condition also implies that the magnetostatic limit always holds: the ratio $B_\star M_a/\dot{M}_a \gg \pi^{3/2} R_\star \rho_{R_\star}^{1/2} \approx 2 \times 10^8$ G s, and from Tables 1 and 2, $B_\star M_a/\dot{M}_a \approx B_\star T_a \gtrsim 3 \times 10^9$ G s.

For mountains grown on a hard surface, we additionally set the velocity $\boldsymbol{v}(t, r, \theta)$ within the injection region, such that the accreted matter is always given a fixed speed $v_{\text{inj}} = 10^{-4}\ c_s$ parallel to the magnetic field $\boldsymbol{B}(t, r, \theta)$. The value of v_{inj} should be a small fraction of the escape speed $v_{\text{esc}} \approx 4.1c_s$, so there is negligible mass lost through the outer boundary (see Section 3.2). We find that setting $\boldsymbol{v}$ carefully is critical to stability.

Table 3. List of important physical parameters of accreting neutron stars (top part), and a summary of the results of the simulations presented in this paper (bottom part).

Quantity	Value/Range	Reference
Accreted mass	10^{-4}–$0.8\,M_\odot$	1, 2, 4
Accretion time-scale	10^4–10^6 yr	1, 7
Density of crust	10^9–10^{14} g cm $^{-3}$	5, 10
Depth of crust	∼1000 m	5, 10
Initial magnetic field	10^{12}–10^{13} G	3, 8, 9
Temperature	10^8–10^9 K	6, 10
Ellipticity	5×10^{-5}–2×10^{-4}	11
Effect of sinking	ϵ reduced by 25–60 per cent	11

References: 1. Taam & van den Heuvel (1986); 2. van den Heuvel & Bitzaraki (1995); 3. Hartman et al. (1997); 4. Wijers (1997); 5. Brown & Bildsten (1998); 6. Brown (2000); 7. Cumming et al. (2001); 8. Arzoumanian, Chernoff & Cordes (2002); 9. Faucher-Giguère & Kaspi (2006); 10. Chamel & Haensel (2008); 11. This work.

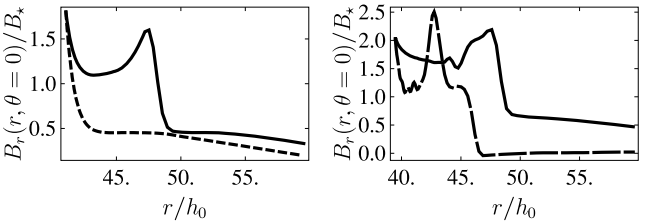

Figure 3. Radial component of the magnetic field B_r along $\theta = 0$: for simulation $\mathcal{S}(R_\star, 10^2)$ (left-hand panel), at $t = 0.45T_a$ (solid) and $t = 0.85T_a$ (dotted); and for simulation $\mathcal{S}(R_\star, 10^3)$ (right-hand panel), at $t = 0.24T_a$ (solid), and its time of failure $t = 0.35T_a$ (dashed).

3 COMPARING MOUNTAINS GROWN ON HARD AND SOFT BASES

Table 2 lists the parameters of the simulations presented in this paper. Mountains grown on a hard surface are labelled $\mathcal{H}(M_a/M_c)$. Mountains grown on a fluid base are labelled $\mathcal{S}(r_{\text{inj}}, M_a/M_c)$, where the injection radius r_{inj} may be either $r_{\min}$ or $R_\star$. The parameters of each run are chosen to grow a mountain with a particular target mass, M_a. We choose four values for M_a in the range 10^{-4}–$10^{-1}\,M_\odot$. These values are chosen to demonstrate the ability of the injection procedure to generate stable mountains over a wide range of masses. This range also encompasses the range of M_a of real accreting neutron stars (see Table 3). The main source of uncertainty is the accretion efficiency (van den Heuvel & Bitzaraki 1995), which may be as low as ∼5 per cent (Tauris, van den Heuvel & Savonije 2000); this is reflected in the chosen range of M_a.

The CPU time required for each run was, on average, $\sim 10^{-2}$ s per grid cell per unit t_0 of simulation time. For $\mathcal{S}(R_\star)$-type simulations, one must scale T_a with M_a to prevent numerical instabilities. Even so, run $\mathcal{S}(R_\star, 10^3)$ does not complete; ZEUS-MP aborts at $t \approx 0.35T_a$, when the adaptive time-step shrinks below its allowed minimum. Fig. 3 shows that this behaviour arises when B_r diverges at $r \lesssim r_{\text{inj}}$ along the boundary $\theta = 0$: for $M_a = 10^2 M_c$, B_r threatens to break out for $t \lesssim 0.5T_a$ but ultimately settles down to the equilibrium configuration before $t = T_a$, whereas for $M_a = 10^3 M_c$, it grows uncontrollably up to the time of failure.

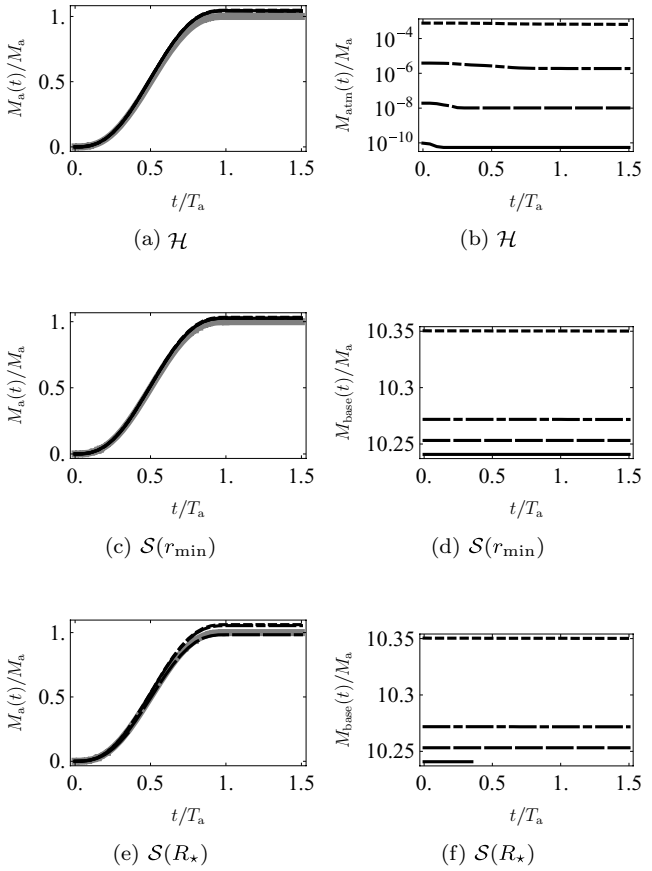

Figure 4. Accreted mass $M_a(t)$ and masses in the stellar atmosphere $M_{atm}(t)$ and fluid base $M_{base}(t)$, plotted in black, for $M_a/M_c = 1$ (dotted), 10 (dot–dashed), 10^2 (dashed) and 10^3 (solid). The injected mass from equation (3) is overplotted in grey. The labels beneath each panel indicate a hard-surface ($\mathcal{H}$) or soft-surface [$\mathcal{S}(r_{min})$ or $\mathcal{S}(R_\star)$] run; see Table 2. The short solid line at the bottom of Fig. (f) is from the aborted run $\mathcal{S}(R_\star, 10^3)$.

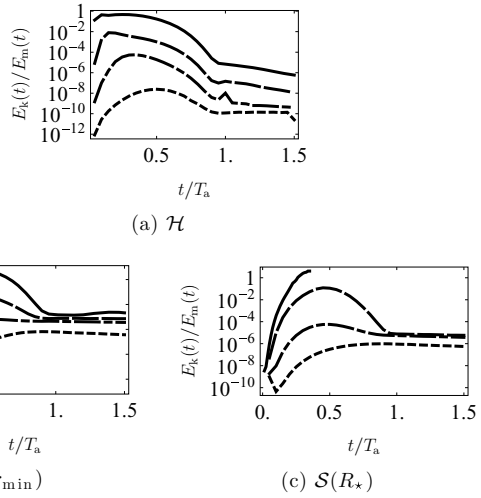

Figure 5. Kinetic energy $E_k(t)$, normalized by the magnetic energy $E_m(t)$, for $M_a/M_c = 1$ (dotted), 10 (dot–dashed), 10^2 (dashed) and 10^3 (solid). The labels beneath each panel indicate a hard-surface ($\mathcal{H}$) or soft-surface [$\mathcal{S}(r_{min})$ or $\mathcal{S}(R_*)$] run; see Table 2.

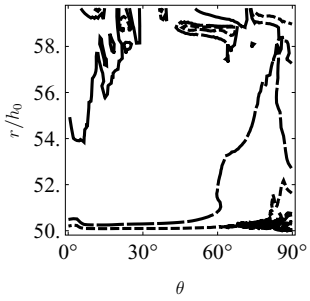

Figure 6. Contours of the absolute, normalized divergence of $\boldsymbol{B}$ of mountain $\mathcal{H}(10^3)$ at $t = T_a$. Contour levels are at 5×10^{-2} (solid), 10^{-2} (dashed), 5×10^{-3} (dotted).

3.1 Verification

We first check that, for each mountain (i) we accumulate the correct total mass M_a, with minimal loss through the outer boundary; (ii) the mass above the surface, M_{atm}, remains much smaller than M_a and (iii) for mountains with sinking, the mass in the fluid base, M_{base}, remains large compared to M_a, so that the magnetic line-tying condition at $r = r_{min}$ is a good approximation. Figs 4(a), (c) and (e) show $M_a(t) = \int_V \mathrm{d}V\,\rho X_a$ integrated over the simulation volume V at time t. We see that the mountains achieve their target mass, which remains in the simulation for $t > T_a$. The injected mass $M_a(t)/M_a$, found by integrating equation (3) with respect to time, is plotted alongside in grey; the two curves overlap. Fig. 4(b) shows M_{atm} for the hard-surface experiment; it is always small. Figs 4(d) and (f) show M_{base} for the soft-surface experiments; it always exceeds $\approx 10 M_a$, as desired. For all simulations where $M_{base} > 0$, the total fraction of M_{base} lost through the outer boundary is $\ll 0.01$ per cent, consistent with Vigelius & Melatos (2008).

We next check that accretion takes place in the magnetostatic limit, i.e. that the total kinetic energy $E_k = \int_V \mathrm{d}V\,\rho|\boldsymbol{v}|^2/2$ is small compared to the total magnetic energy $E_m = \int_V \mathrm{d}V|\boldsymbol{B}|^2/(8\pi)$. Fig. 5 shows the ratio of E_k to E_m as a function of time. We see that E_k/E_m tends to increase with M_a but typically never rises above 1 per cent, except in $\mathcal{H}(10^3)$ and the incomplete run $\mathcal{S}(r_{min}, 10^3)$. After accretion stops, at $t = T_a$, E_k/E_m typically falls to less than 10^{-4}.

Magnetic field transport in ZEUS-MP is divergence-free by construction (Hayes et al. 2006), but it is worth checking whether this property is preserved by the injection algorithm. We find that the mean value of $|\nabla \cdot \boldsymbol{B}|/\sum_i(|B_i|/dx^i)$ is initially $\lesssim 6 \times 10^{-3}$, and increases by a factor of 3.5 at most over the run. Fig. 6 shows contours of the normalized $|\nabla \cdot \boldsymbol{B}|$ for an illustrative mountain.

3.2 Illustrative example

We choose mountain $\mathcal{H}(10^2)$, grown on a hard surface with $M_a = 10^2 M_c$, to illustrate the general evolution of a magnetic mountain during accretion. The top row of Fig. 7 shows contours of the mountain density ρX_a, normalized by the initial surface density $\rho_{R_\star}$, at four different times. The lower row shows the magnetic flux ψ, normalized by $\psi_\star = B_\star R_\star^2/2$, at the same times. Matter is added predominately at the pole, as determined by $\mathrm{d}M/\mathrm{d}\psi$. In the early stages of accretion ($t = 0.1T_a$), the magnetic field is only slightly disturbed. As accretion progresses, the mountain spreads towards the equator, dragging the frozen-in magnetic field with it. The angular span of the ψ contours is compressed from $\sim 70^\circ$ [Fig. 7(e)] to $\sim 20^\circ$ [Fig. 7(f)]. At the half-way point ($t = 0.5T_a$), the flux is significantly displaced from its initial configuration, but

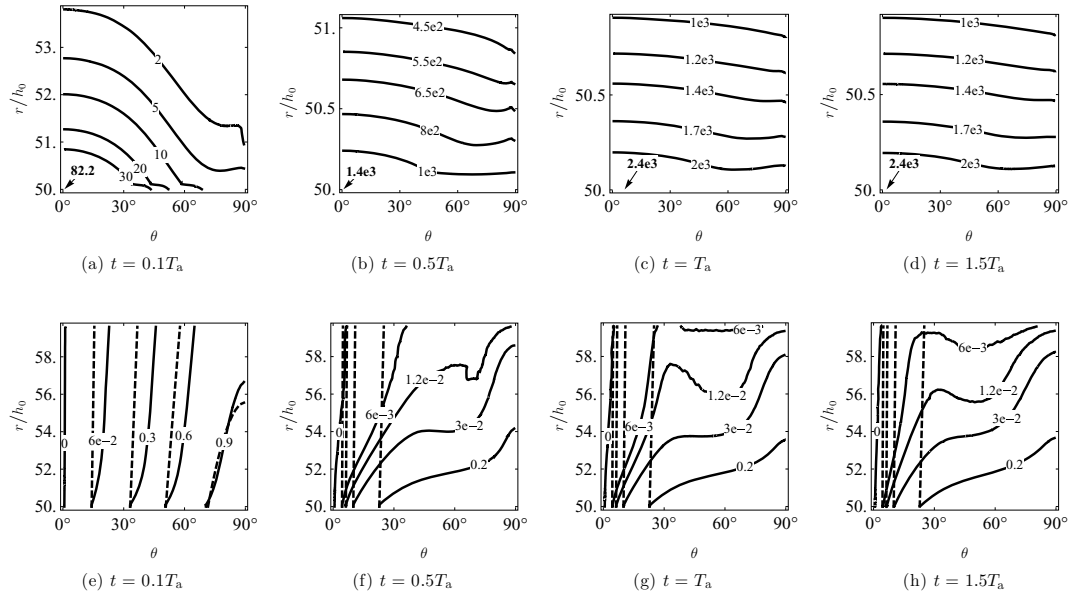

(a) $t = 0.1T_{\rm a}$ (b) $t = 0.5T_{\rm a}$ (c) $t = T_{\rm a}$ (d) $t = 1.5T_{\rm a}$

(e) $t = 0.1T_{\rm a}$ (f) $t = 0.5T_{\rm a}$ (g) $t = T_{\rm a}$ (h) $t = 1.5T_{\rm a}$

Figure 7. Hydromagnetic structure of hard-surface mountain $\mathcal{H}(10^2)$ at times $t/T_{\rm a} = 0.1$, 0.5, 1.0 and 1.5. (Top row) Contours of accreted density $\rho X_{\rm a}/\rho_{R_\star}$; the maximum is indicated with a small arrow and labelled in bold. (Bottom row) Contours of magnetic flux $\psi/\psi_\star$, at the labelled times (solid), and at $t = 0$ (dashed). The dotted contours meet their solid equivalents on the left vertical axis. Note that the scale of the r axis differs between Figs (a) and (d). The change in the contour scale between Fig. (e) and Figs (f)–(h) is due to the difference in ψ between $t = 0$, where the magnetic field is dipolar, and subsequent times when the magnetic field is distorted.

remains anchored to the inner boundary at $r = r_{\rm min}$, demonstrating magnetic line tying. We see, in the $\psi/\psi_\star = 1.2 \times 10^{-2}$ contour, the early formation of the magnetic 'tutu' configuration, observed in Payne & Melatos (2004, 2007) for $M_{\rm a} = 10^{-5}\,{\rm M}_\odot$.

At $t = T_{\rm a}$, the mountain reaches its target mass ($M_{\rm a} = 10^2 M_{\rm c}$ in Fig. 7). Despite sliding towards the equator, the accreted matter still exhibits a notable variation in density with respect to θ; a polar mountain is formed. The tutu configuration of the magnetic field is clearly visible; see for comparison figs 2 and 4(a) of Payne & Melatos (2004). This equilibrium state remains largely unchanged when we run the simulation for an additional $0.5T_{\rm a}$, during which no further mass is added.

3.3 Sinking

We next compare the hard-surface equilibrium state, illustrated in Figs 7(c) and (g), with the two experiments where we include sinking. Fig. 8 shows contours of $\rho X_{\rm a}$ and ψ in each of the three scenarios, with $M_{\rm a} = 10M_{\rm c}$. The hard-surface mountain [Fig. 8(a)] spreads appreciably, and the magnetic flux [Fig. 8(d)] is significantly displaced towards the equator. The density contour $\rho X_{\rm a}/\rho_{R_\star} = 10$ begins a distance $\sim 4h_0 = 215$ cm (see Table 1) above the injection radius $r = r_{\rm min} = R_\star$ at the pole and sinks below the equator to $\sim$75 per cent of the polar height of the mountain. In contrast, the same contour of the sinking mountain grown at $r = r_{\rm min}$ [Fig. 8(b)] begins $\sim 0.6h_0$ above the injection radius $r = r_{\rm min}$ at the pole and sinks below the equator to just $\sim$19 per cent of the polar height of the mountain. From the $\rho X_{\rm a}/\rho_{R_\star} = 10^{-3}$ contour, we see that the accreted matter is confined to $r - r_{\rm min} \lesssim 0.7h_0$ above the inner boundary at the pole and $r - r_{\rm min} \lesssim 0.15h_0$ at the equator.

In short, the sunk mountain grown at $r = r_{\rm min}$ hugs the inner boundary and pole, and resembles the initial mass distribution seen in Fig. 7(a). This is not surprising. Matter is fed in at $r = r_{\rm min}$ with zero velocity, as discussed in Section 2.1. It expands outward due to the pressure gradient created as matter piles up at the injection radius; since we are injecting quasi-statically, the pressure gradient is small. On the other hand, the weight of the massive overburden ($M_{\rm base} \approx 10M_{\rm a}$) presses down on the added material. The magnetic flux is displaced [Fig. 8(e)], but much less than for the hard mountain. Field lines remain tied to the inner boundary, bending away in its immediate vicinity (because the slug of injected matter does not rise). Above this layer, the field lines of the initial and final states remain largely parallel.

The structure of the sunk mountain grown at $r = R_\star$ [Fig. 8(c)] differs from the other two cases. The contour $\rho X_{\rm a}/\rho_{R_\star} = 10$, tracked above, starts at the pole, remains virtually flat at $\sim 2h_0$ below the injection radius, bends sharply inward near the equator, moves directly towards the inner boundary, then curves back towards the pole, crossing it again at $\sim 6h_0$ below the injection radius. For the previous two mountains, grown from $r = r_{\rm min}$, the angular variation in density increases with altitude. Here, the reverse is true: the angular variation density decreases with increasing r, up until $r \lesssim R_\star$, with the greatest variation within $\sim 4h_0$ of the inner boundary. While the two sinking scenarios differ in their final distributions of accreted (as opposed to total) density, their final distributions of magnetic flux [Figs 8(e) and (f)] are very similar.

The mountain sinks three times further into the fluid base at the pole than at the equator. This is consistent with how mass is injected according to equation (4); the input flux is $\sim$20 times greater at the pole than at the equator. In addition, the magnetic field guides accreted matter sideways as field lines flatten across the surface towards the equator, whereas matter at the pole can sink inward readily along almost vertical flux tubes [e.g. the contour $\psi/\psi_\star = 6 \times 10^{-2}$ in Fig. 8(f)].

The density contours bunch together along the underside of the mountain, spanning five orders of magnitude; the injected matter does not sink below this boundary. The lowest of the bunched density contours, $\rho X_{\rm a}/\rho_{R_\star} = 10^{-3}$, never reaches the inner boundary; the mountain is floating in isostatic equilibrium with the surrounding fluid base. The contour rises to only $\sim 1h_0$ above $R_\star$ at the

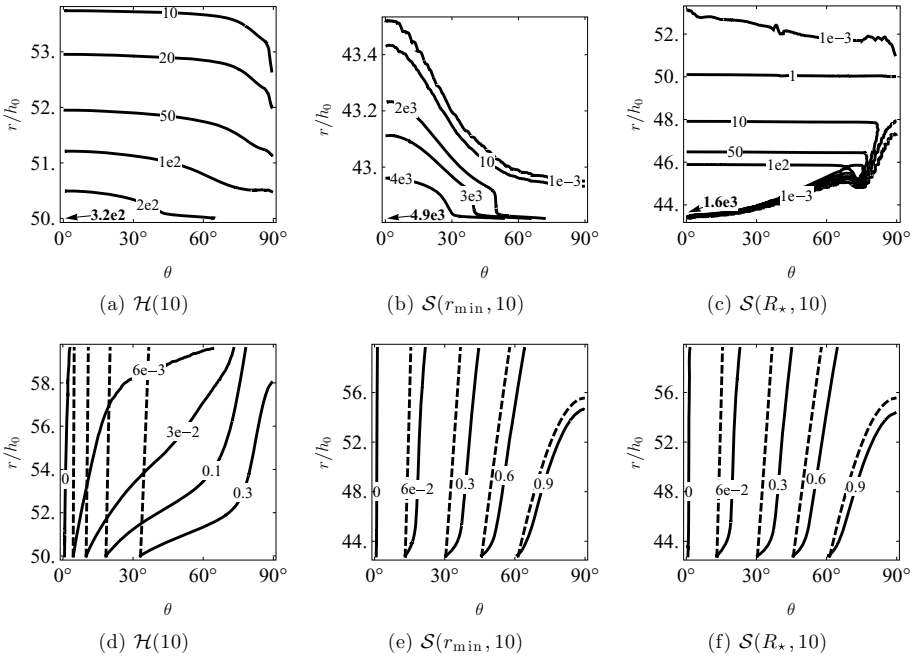

(a) $\mathcal{H}(10)$ (b) $\mathcal{S}(r_{\rm min}, 10)$ (c) $\mathcal{S}(R_\star, 10)$

(d) $\mathcal{H}(10)$ (e) $\mathcal{S}(r_{\rm min}, 10)$ (f) $\mathcal{S}(R_\star, 10)$

Figure 8. Comparison of the hydromagnetic structure of hard- and soft-surface mountains. Contours of accreted density $\rho X_{\rm a}/\rho_{R_\star}$ (top row) and magnetic flux $\psi/\psi_\star$ (bottom row) of mountains $\mathcal{H}(10)$, $\mathcal{S}(r_{\rm min}, 10)$ and $\mathcal{S}(R_\star, 10)$, at time $t = T_{\rm a}$. Details are as for Fig. 7. Note that the scale of the r axis differs between Figs (a) and (c), and between Figs (d) and (f).

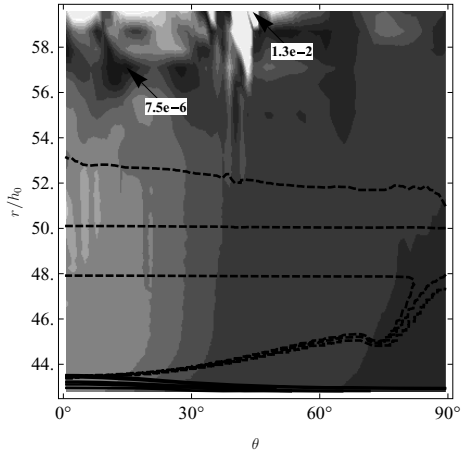

Figure 9. Shaded contours of the absolute, normalized difference in total density ρ between $\mathcal{S}(r_{\rm min}, 10)$ and $\mathcal{S}(R_\star, 10)$, overlaid with the $\rho X_{\rm a}$ (accreted only) contours of Figs 8(b) and (c) (solid and dashed, respectively). The minimum and maximum density differences are indicated with small arrows and labelled in bold.

equator and $\sim 3h_0$ at the pole; in contrast it reaches $R_\star - r \lesssim 6h_0$ at the pole. The path of this contour, if overlaid on Fig. 8(a), would trace densities between 2×10^{-3} and $50\rho_{R_\star}$. Finally, note that 0.3 per cent of the mountain mass is above the stellar surface. Compared to the other two scenarios, the structure of $\mathcal{S}(R_\star, 10)$ is perhaps more reminiscent of an 'iceberg'.

Ultimately, we are interested in the final distribution of the total mass, that is, the accreted matter, $\rho X_{\rm a}$, plus the fluid base it displaces, $\rho(1 - X_{\rm a})$. Does injection at $r_{\rm min}$ or $R_\star$ make a difference? Fig. 9 displays the absolute, normalized difference $|\rho_{r_{\rm min}} - \rho_{R_\star}|/|\rho_{r_{\rm min}} + \rho_{R_\star}|$ between the total densities in the two sinking scenarios as a grey-scale plot. The largest differences occur at $r > R_\star$, where there is little mass, and are therefore unimportant. For $r < R_\star$, the difference peaks near the pole but remains less than $\sim$0.8 per cent. In other words, despite the difference in the final distribution of ρ X $_{\rm a}$ between the two injection scenarios (emphasized by the overlaid contours), the final distribution of ρ is essentially the same. Injecting at $r_{\rm min}$ or $R_\star$ makes no difference because the soft base readjusts in each case to yield the same overall equilibrium state. This is an important result. It confirms the robustness of the injection method and the argument presented in Section 2.1: in ideal MHD, the equilibrium state is independent of precisely where matter is initially injected. In practice, injection at $r_{\rm min}$ seems preferable because it reduces the simulation time (see Table 2) and improves numerical stability, as illustrated by the failure of run $\mathcal{S}(R_\star, 10^3)$.

3.4 Magnetic line tying

Finally, we investigate the assumption of magnetic line tying. In Fig. 10, we plot the angle $\beta(r, \theta) = \sin^{-1}(B_\theta/|\boldsymbol{B}|)$ between the magnetic field $\boldsymbol{B}$ and the radial unit vector as a function of θ at $r = r_{\rm min}$ and $r = R_\star$. We also plot β at the inner boundary of a Grad-Shafranov mountain with $M_{\rm a} = M_{\rm c}$ (Payne & Melatos 2004), and β for a dipole (independent of radius). The $\mathcal{S}(R_\star)$ mountains give the same results as $\mathcal{S}(r_{\rm min})$.

The hard-surface mountains in Fig. 10(a) behave like the Grad–Shafranov mountain at low $M_{\rm a}$ but become increasingly dipolar as $M_{\rm a}$ increases. This is expected; at low $M_{\rm a}$, the accreted mass stays close to the pole and distorts the magnetic field there. As $M_{\rm a}$ increases, the mountain spreads over a greater volume, and the magnetic field is distorted less at any particular point. The sign inversion close to the equator may be caused by numerical reconnection, or by the reflective boundary condition at $\theta = \pi/2$; further tests with a resisitive ideal-MHD solver are needed to make sure.

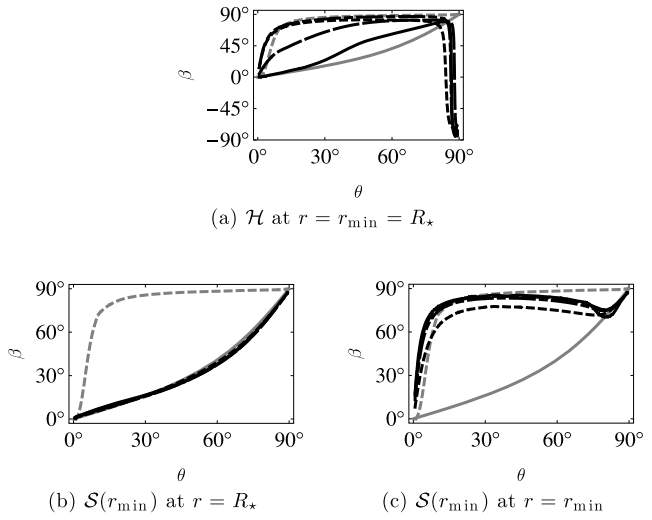

Figure 10. Angle between the magnetic field $\boldsymbol{B}$ and the radial unit vector, plotted versus colatitude θ at (a) $r = r_{\rm min} = R_\star$, (b) $r = R_\star$ and (c) $r = r_{\rm min}$, for $M_{\rm a}/M_{\rm c} = 1$ (dotted), 10 (dot–dashed), 10^2 (dashed) and 10^3 (solid). Results from this paper are plotted in black. Plotted in grey are $\beta(r, \theta)$ for a Payne & Melatos (2004) Grad–Shafranov mountain (dotted), and for a dipole (solid).

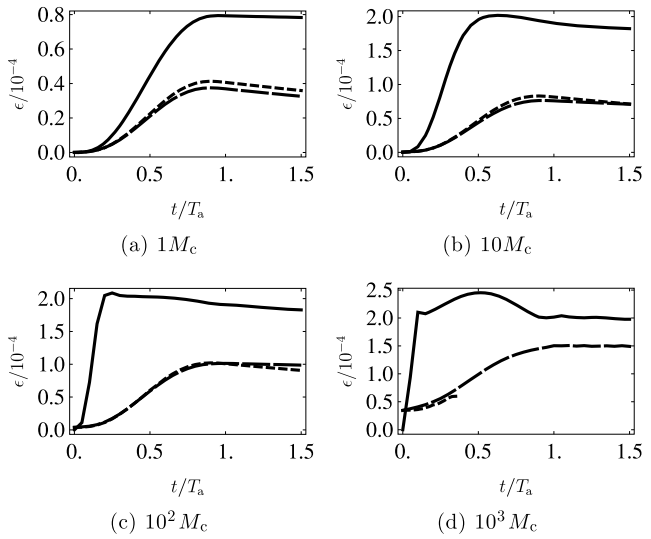

Figure 11. Ellipticity as a function of time, for $M_{\rm a}/M_{\rm c} = 1, 10, 10^2, 10^3$ (top left to bottom right), and for mountains $\mathcal{H}$ (solid), $\mathcal{S}(r_{\rm min})$ (dashed) and $\mathcal{S}(R_\star)$ (dotted).

The soft-surface mountains in Fig. 10(b) are dipolar at $r = R_\star$, as expected, but at $r = r_{\rm min}$ [Fig. 10(c)] they more closely resemble the Grad-Shafranov mountain. One might expect β to closely match a dipole at $r = r_{\rm min}$, given that the magnetic field lines are tied there, and we choose $M_{\rm base} \gg M_{\rm a}$ in order to minimize sideways fluid displacements at the bottom of the soft base. It is unclear whether the magnetic distortions are artificial, because the injected slug matter enters from below and cannot expand upwards to match accretion from above (see Section 5 for further discussion). Alternatively, kinks in the magnetic field may be communicated rapidly down to arbitrary depths by Alfvén waves, even though the Alfvén speed $\propto \rho^{-1/2}$ decreases rapidly with depth. If so, the high breaking strain of the solid, conducting crust (Horowitz & Kadau 2009) assumes even greater importance in enforcing line tying.

We argued, in Section 2.1, that the final equilibrium state of the mountain is independent of $r_{\rm inj}$. In general, a given total $M_{\rm a}$ and injected mass flux $\partial M_{\rm a}/\partial\psi$ does not define a *unique* ideal-MHD equilibrium. Matter injected from above spreads sideways faster than it sinks, like a layered cocktail drink, while a slug of matter injected from below forces the base sideways without much movement at the surface [compare Figs 8(c) and (b)]. Conceivably, therefore, ZEUS-MP may converge on different equilibria depending on $r_{\rm inj}$. The results of Section 3.3 engender confidence that the mountain structure does not depend on $r_{\rm inj}$; the issue is not definitively settled, however, for the following subtle reason.[4]

Consider a polar field line in the bottom row of Fig. 7. As accretion proceeds, it bends towards the equator until it touches the corner $(r, \theta) = (r_{\rm max}, \pi/2)$. At that point, it instantaneously snaps through some nonzero angle, from $B_r \neq 0$ (free boundary at $r = r_{\rm max}$) to $B_r = 0$ (reflecting boundary at $\theta = \pi/2$). Effectively, this corresponds to a dissipative, reconnection-like event occurring just *outside* the simulation volume, artificially pinching off magnetic loops.[5] Such a process is irreversible. Furthermore, it acts differently on the sequence of quasi-static equilibria that ZEUS-MP hypothetically passes through during slow accretion from above and below because sideways spreading happens at different altitudes in the two cases.

In the runs presented in this paper, the density in the vicinity of the corner $(r_{\rm max}, \pi/2)$ is tiny, as is the mass efflux through the boundary $r = r_{\rm max}$ (see Section 3.1). One can therefore argue plausibly that the irreversible dissipation at $(r_{\rm max}, \pi/2)$, while it exists in principle, does not significantly affect the final state. There is a chance, however, that if one adds material slowly from above, reconnection (where numerical or real) pinches off one small magnetic loop after another at the equator, as in the Earth's magnetotail. Resisitive MHD simulations by Vigelius & Melatos (2009b) do not show such behaviour, but they mostly started from preformed Grad–Shafranov equilibria instead of growing the mountain from scratch. A more careful consideration of this issue is required for future simulations.

4 MASS QUADRUPOLE MOMENT

The distorted hydromagnetic equilibria in Section 3 have an associated mass quadrupole moment, with principal axis along the pre-accretion magnetic axis, which is quantified in terms of the ellipticity

$$\epsilon = \frac{\pi}{I_{zz}} \int_{r_{\rm min}}^{r_{\rm max}} {\rm d}r\, r^4 \int_0^{\pi/2} {\rm d}\theta\, \sin\theta (3\cos^2\theta - 1)\, \rho(t, r, \theta)\,, \qquad (5)$$

with $I_{zz} = 2M_\star R_\star^2/5$. Fig. 11 shows ϵ with respect to time as the mountain grows. All mountains achieve a non-zero ellipticity at $t = T_{\rm a}$, which decreases negligibly thereafter, confirming the mountains are stable. The time taken for the hard-surface mountains to converge to their equilibrium values of ϵ decreases with $M_{\rm a}$, from $\sim T_{\rm a}(M_{\rm a} = 1M_{\rm c})$ to $\sim 0.1T_{\rm a}(M_{\rm a} = 10^3 M_{\rm c})$; this is consistent with

[4] Sterl Phinney, private communication.

[5] The effect can be magnified in ZEUS-MP by increasing the cell size close to $r = r_{\rm max}$; eventually ZEUS-MP aborts when B_r diverges close to the $(r_{\rm max}, \pi/2)$ corner.

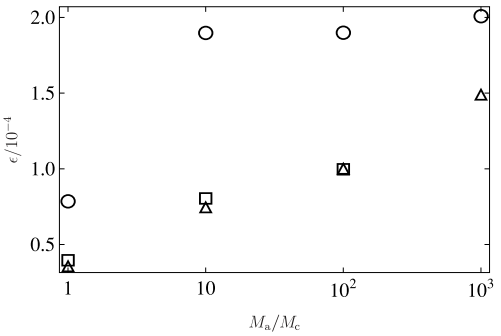

Figure 12. Ellipticity as a function of M_a, at time $t = T_a$, for mountains $\mathcal{H}$ (circles), $\mathcal{S}(r_{min})$ (triangles) and $\mathcal{S}(R_\star)$ (squares).

the decreased confinement of the mountain by the magnetic field, i.e. its increased ability to spread. The ellipticities of the soft-surface mountains for the two injection scenarios are virtually identical; even the incomplete run $\mathcal{S}(R_\star, 10^3)$ closely follows $\mathcal{S}(r_{min}, 10^3)$ up until failure. As in Section 3.3, the final density distribution is independent of the injection procedure.

The origin of the uneven behaviour of the ellipticity of $\mathcal{H}(10^3)$ [Fig. 11(d)] is unknown. We note, however, that its functional dependence on t is similar to that of $\dot{M}_a$ (equation 3 and Fig. 2), and therefore it is likely that the rise and fall of the ellipticity is due to the reconfiguration of the $\mathcal{H}(10^3)$ mountain in response to the changing accretion rate. We note similar undulations in the kinetic energies [Figs 5(b) and (c)] and, to a lesser degree, in the ellipticity of $\mathcal{H}(10)$ [Fig. 11(b)].

Fig. 12 shows ϵ (in black) at $t = T_a$ as a function of M_a. The ellipticity of the hard-surface mountains rises by a factor of $\sim$2.5 as M_a increases from 1 to $10M_c$ and flattens thereafter, rising by a further 5 per cent as M_a increases from 10 to $10^3 M_c$. Importantly, accreting further matter does not reduce ϵ; the mountain does not smooth itself out. The ellipticities of the soft-surface mountains rises by $\sim$60 per cent per decade in M_a.

Fig. 12 clearly quantifies the effect of sinking: ϵ decreases, relative to the hard-surface scenario, by $\sim$50 per cent at $M_a = 1M_c$, $\sim$60 per cent at $M_a = 10M_c$, and $\sim$25 per cent at $M_a = 10^3 M_c$.

5 DISCUSSION

In this paper, we simulate the growth of magnetically confined mountains on an accreting neutron star, with realistic masses $M_a \lesssim 0.12\,M_\odot$, under the two scenarios where the mountain sits on a hard surface and sinks into a soft, fluid base. In the latter scenario, we confirm that the final equilibriun state is independent of the altitude where matter is injected. We find that the ellipticity of a hard-surface mountain does not increase appreciably for $M_a \gtrsim 10M_c$, saturating at $\sim 2 \times 10^{-4}$, whereas the ellipticity of a soft-surface mountain continues to increase from $M_a = 10$ to $10^3 M_c$. Sinking reduces the ellipticity by up to 60 per cent relative to the hard-surface value.

Choudhuri & Konar (2002) developed a kinematic model of accretion, which treats sinking in a different (but complementary) way to this paper. An axisymmetric magnetic field is evolved under the influence of a *prescribed* velocity field, which models the flow of accreted matter from pole to equator, where it submerges and moves towards the core (see their fig. 1). Ohmic diffusion is included, but, for a subset of the results (where the resistivity $\eta = 0.01$), it is negligible, permitting a direct comparison with this paper.

Fig. 5 of Choudhuri & Konar (2002) shows the evolved configuration of an initially dipolar field which permeates the entire star. We compare to Figs 8(e) and (f) of this paper. In both models, the magnetic field is distorted significantly by accreted matter spreading towards the equator ($r_m < r < r_s$ in Choudhuri & Konar; the entire simulation in this paper). In Choudhuri & Konar's work, the magnetic field is completely submerged beneath the surface and confined to the zone where the submerged accreted matter flows back towards the pole. In this paper, magnetic field lines still penetrate the surface, implying less effective screening. Within the core, Choudhuri & Konar's magnetic field remains relatively undisturbed. Magnetic line-tying is not enforced, but the prescribed radial flow within the core naturally restricts the sideways displacement of the magnetic field there. If there were sideways motion of the matter within the core, it would modify the degree of magnetic screening, but neither our simulations nor the results of Choudhuri & Konar show evidence for such motion. Extending our simulations deeper into the star to include the core and explore this possibility properly would be a technical challenge; for instance, we would need to incorporate a more realistic equation of state and track even more disparate equilibrium time-scales.

To explain the narrow range in the rotation frequencies of low-mass X-ray binaries (Chakrabarty et al. 2003), it is proposed that the stars radiate angular moment in gravitational waves at a rate which balances the accretion torque (Wagoner 1984; Bildsten 1998). Magnetic mountains are one of a number of physical mechanisms proposed for the associated permanent quadrupole; see Vigelius & Melatos (2009a) and references therein. The relationship between ϵ and the rotation frequency f predicted by torque balance is $f \propto \epsilon^{-2/5}$. Thus, the 25–60 per cent reduction in ϵ due to sinking calculated in this paper increases f by 12–44 per cent, all other things being equal. This goes some way towards bringing magnetic mountain ellipticities down to a level consistent with the data, but there is still a long way to go. Observations to date have found $45\,\mathrm{Hz} < f < 620\,\mathrm{Hz}$ for burst oscillation sources and $182\,\mathrm{Hz} < f < 598\,\mathrm{Hz}$ for accreting millisecond pulsars, implying $6.6 \times 10^{-9} \lesssim \epsilon \lesssim 4.6 \times 10^{-6}$ and $7.2 < 10^{-9} \lesssim \epsilon \lesssim 1.4 \times 10^{-7}$, respectively. Conversely, the ellipticities of sunk mountains calculated in this paper, $3.5 \times 10^{-5} \lesssim \epsilon \lesssim 1.5 \times 10^{-4}$, imply $11\,\mathrm{Hz} \lesssim f \lesssim 20\,\mathrm{Hz}$. Clearly, other relaxation mechanisms, like Ohmic diffusion, must also be playing an important role in reducing ϵ, as the observed f require.

The reduction in ϵ by sinking also reduces the gravitational wave strain (e.g. Abbott et al. 2007), $h \propto \epsilon f^2$, by 6–17 per cent. This is unlikely, by itself, to rule out the detection of gravitational waves from low-mass X-ray binaries by ground-based interferometric detectors; assuming the signal can be coherently integrated, the loss in h can be compensated for by an increase in the observation time $\propto h^{-2}$ of 13–45 per cent. Other difficulties associated with the detection of gravitational waves from low-mass X-ray binaries, such as poorly known orbital parameters and accretion-induced phase wandering (Watts et al. 2008), are likely to be more important.

ACKNOWLEDGMENTS

The authors are grateful for supercomputing time allocated on the Australian NCI National Facility (http://nf.nci.org.au). KW was supported by an Australian Postgraduate Award.

REFERENCES

Abbott B. et al., 2007, Phys. Rev. D, 76, 082001
Arzoumanian Z., Chernoff D. F., Cordes J. M., 2002, ApJ, 568, 289
Bildsten L., 1998, ApJ, 501, L89

Bisnovatyi-Kogan G. S., Komberg B. V., 1974, SvA, 18, 217
Blondin J. M., Freese K., 1986, Nat, 323, 786
Brown E. F., 2000, ApJ, 531, 988
Brown E. F., Bildsten L., 1998, ApJ, 496, 915
Chakrabarty D., Morgan E. H., Muno M. P., Galloway D. K., Wijnands R., van der Klis M., Markwardt C. B., 2003, Nat, 424, 42
Chamel N., Haensel P., 2008, Liv. Revs. Rel., 11
Choudhuri A. R., Konar S., 2002, MNRAS, 332, 933
Cumming A., 2005, in Rasio F. A., Stairs I. H., eds, ASP Conf. Ser. Vol. 328, Binary Radio Pulsars. Astron. Soc. Pac., San Francisco, p. 311
Cumming A., Zweibel E., Bildsten L., 2001, ApJ, 557, 958
Cumming A., Arras P., Zweibel E., 2004, ApJ, 609, 999
Faucher-Giguère C.-A., Kaspi V. M., 2006, ApJ, 643, 332
Goedbloed J. P. H., Poedts S., 2004, Principles of Magnetohydrodynamics. Cambridge Univ. Press, Cambridge
Hameury J. M., Bonazzola S., Heyvaerts J., Lasota J. P., 1983, A&A, 128, 369
Hartman J. W., Bhattacharya D., Wijers R., Verbunt F., 1997, A&A, 322, 477
Hayes J. C., Norman M. L., Fiedler R. A., Bordner J. O., Li P. S., Clark S. E., ud Doula A., Mac Low M.-M., 2006, ApJS, 165, 188
Horowitz C. J., Kadau K., 2009, Phys. Rev. Lett., 102, 191102
Konar S., Bhattacharya D., 1997, MNRAS, 284, 311
Konar S., Bhattacharya D., 1999, MNRAS, 308, 795
Konenkov D., Geppert U., 2001, MNRAS, 325, 426
Kosiński R., Hanasz M., 2006, MNRAS, 368, 759
Lovelace R. V. E., Romanova M. M., Bisnovatyi-Kogan G. S., 2005, ApJ, 625, 957
Melatos A., Phinney E. S., 2001, PASA, 18, 421
Payne D. J. B., Melatos A., 2004, MNRAS, 351, 569
Payne D. J. B., Melatos A., 2007, MNRAS, 376, 609
Rheinhardt M., Geppert U., 2002, Phys. Rev. Lett., 88, 101103
Romani R. W., 1990, Nat, 347, 741
Romanova M. M., Kulkarni A. K., Lovelace R. V. E., 2008, ApJ, 673, L171
Ruderman M., Zhu T., Chen K., 1998, ApJ, 492, 267
Srinivasan G., Bhattacharya D., Muslimov A. G., Tsygan A. J., 1990, Curr. Sci., 59, 31
Stone J. M., Norman M. L., 1992a, ApJS, 80, 753
Stone J. M., Norman M. L., 1992b, ApJS, 80, 791
Taam R. E., van den Heuvel E. P. J., 1986, ApJ, 305, 235
Tauris T. M., van den Heuvel E. P. J., Savonije G. J., 2000, ApJ, 530, L93
Urpin V., Geppert U., Konenkov D., 1998, MNRAS, 295, 907
van den Heuvel E. P. J., Bitzaraki O., 1995, A&A, 297, L41
Vigelius M., Melatos A., 2008, MNRAS, 386, 1294
Vigelius M., Melatos A., 2009a, MNRAS, 395, 1972
Vigelius M., Melatos A., 2009b, MNRAS, 395, 1985
Wagoner R. V., 1984, ApJ, 278, 345
Watts A. L., Krishnan B., Bildsten L., Schutz B. F., 2008, MNRAS, 389, 839
Wijers R. A. M. J., 1997, MNRAS, 287, 607
Zhang C. M., Kojima Y., 2006, MNRAS, 366, 137

APPENDIX A: MATCHING A FLUID BASE TO A GRAD–SHAFRANOV MOUNTAIN IN ZEUS-MP

We attempted to incorporate a fluid base into the framework of Payne & Melatos (2007) and Vigelius & Melatos (2008) in the following ad hoc manner. Starting with a Grad–Shafranov equilibrium loaded into ZEUS-MP, we extend the inner simulation boundary, initially at $r = R_\star$, inwards to create a region $r_{\rm min} < r < R_\star$, containing the fluid base. The magnetic field $\boldsymbol{B}$ in this region is initialized to a dipole. At $r = R_\star$, B_r matches perfectly, but B_θ is discontinuous (see, e.g. fig. 2 of Payne & Melatos 2004). The initial density $\rho(t = 0, r, \theta)$ is chosen to match the Grad–Shafranov density $\rho_{\rm GS}(r, \theta)$ at $r = R_\star$, and to match an isothermal, non-self-gravitating profile within $r < R_\star$. A number of ad hoc choices of $\rho(t = 0, r, \theta)$ were tried, e.g. the maximum of $\rho_{\rm GS}(R_\star, \theta)$ and $\rho'_{R_\star} \exp[GM_\star(r^{-1} - R_\star^{-1})/c_{\rm s}^2]$, with $\rho'_{R_\star} = \min_\theta \rho_{\rm GS}(R_\star, \theta)$. When the combined Grad–Shafranov mountain and fluid base are evolved in ZEUS-MP, the results are undesirable. Except when $R_\star - r_{\rm min} \ll h_0$, the fluid base is sufficiently far from equilibrium to completely disrupt the Grad–Shafranov mountain, which collapses over a short time-scale $\sim t_0$.

APPENDIX B: LOGARITHMIC RADIAL GRID SPACING

The logarithmic grid spacing in r is determined as follows. The $N_r + 1$ radial cell boundaries $r_{\rm min} = r_0, r_1, r_2, \ldots, r_{N_r} = r_{\rm max}$ are given by $r_{n+1} = r_n + \Delta r_n$, where

$$\sum_{n=0}^{N_r-1} \Delta r_n = r_{\rm max} - r_{\rm min}\,, \tag{B1}$$

$$\frac{\Delta r_{n+1}}{\Delta r_n} = \left(\frac{\Delta r_{N_r-1}}{\Delta r_0}\right)^{1/(N_r-1)}\,, \tag{B2}$$

and $\Delta r_{N_r-1}/\Delta r_0$ is the ratio of the maximum to minimum radial grid spacing. The values of $\Delta r_{N_r-1}/\Delta r_0$ used in the simulations presented in this paper are given in Table 2.

APPENDIX C: CUSTOM INJECTION

We add a new subroutine to ZEUS-MP which is called at the beginning of each time-step δt. Within the subroutine, the density $\rho(t, r, \theta)$, mountain concentration $\mathrm{X_a}(t, r, \theta)$, and velocity $\boldsymbol{v}(t, r, \theta)$ of a grid cell within the injection region (at point (r, θ) with size $\delta r \times \delta\theta$) are updated, as follows

$$\rho(t + \delta t, r, \theta) = \rho(t, r, \theta) + \delta\rho(t, r, \theta)\,, \tag{C1}$$

$$\mathrm{X_a}(t + \delta t, r, \theta) = \frac{\rho(t, r, \theta)\mathrm{X_a}(t, r, \theta) + \delta\rho(t, r, \theta)}{\rho(t + \delta t, r, \theta)}\,, \tag{C2}$$

$$\begin{aligned}\boldsymbol{v}(t + \delta t, r, \theta) = {} & v_{\rm inj}\frac{\boldsymbol{B}(t, r, \theta)}{|\boldsymbol{B}(t, r, \theta)|}\mathrm{X_a}(t + \delta t, r, \theta) \\ & + \boldsymbol{v}(t, r, \theta)[1 - \mathrm{X_a}(t + \delta t, r, \theta)]\,.\end{aligned} \tag{C3}$$

The density increment is given by

$$\delta\rho(t, r, \theta) = \frac{M_{\rm a}}{2\pi\delta r\delta\theta}\mathcal{I}(t, r, \theta)\,; \tag{C4}$$

the factor of 2π comes from the size of the grid cell in the ϕ dimension. The function

$$\mathcal{I}(t, r, \theta) = \frac{1}{\mathcal{N}}\int_{t_1}^{t_2}\mathrm{d}t\int_{r_1}^{r_2}\mathrm{d}r\, r^2\int_{\theta}^{\theta+\delta\theta}\mathrm{d}\theta\, \sin\theta\,\frac{\partial^3 M_{\rm a}}{\partial t\partial r\partial\theta}(t, r, \theta) \tag{C5}$$

integrates the injected flux given by equation (2); the constant

$$\mathcal{N} = \int_0^{T_{\rm a}}\mathrm{d}t\int_{r_{\rm inj}}^{r_{\rm inj}+\delta r_{\rm inj}}\mathrm{d}r\, r^2\int_0^{\pi/2}\mathrm{d}\theta\, \sin\theta\,\frac{\partial^3 M_{\rm a}}{\partial t\partial r\partial\theta}(t, r, \theta) \tag{C6}$$

ensures the correct normalization. The times

$$t_1 = \min(t, T_a)\,, \tag{C7}$$

$$t_2 = \min(t + \delta t, T_a)\,, \tag{C8}$$

give the intersection of the current time-step with the injection time interval, and the radii

$$r_1 = \min[\max(r, r_{inj}), r_{inj} + \delta r_{inj}], \tag{C9}$$

$$r_2 = \min[\max(r + \delta r, r_{inj}), r_{inj} + \delta r_{inj}], \tag{C10}$$

give the intersection of the grid cell with the injection region.

This paper has been typeset from a TEX/LATEX file prepared by the author.